Plenoptic projection fluorescence tomography

Ignacio Iglesias[1,*] and Jorge Ripoll[2,3]

[1]*Departmento de Física, Universidad de Murcia, Campus de Espinardo, 30100, Murcia, Spain*
[2]*Department of Bioengineering and Aerospace Engineering, Universidad Carlos III de Madrid, 28911, Madrid, Spain*
[3]*Experimental Medicine and Surgery Unit, Instituto de Investigación Sanitaria Gregorio Marañón, 28007, Madrid, Spain*
[*]*iic@um.es*

Abstract: A new method to obtain the three-dimensional localization of fluorochrome distributions in micrometric samples is presented. It uses a microlens array coupled to the image port of a standard microscope to obtain tomographic data by a filtered back-projection algorithm. Scanning of the microlens array is proposed to obtain a dense data set for reconstruction. Simulation and experimental results are shown and the implications of this approach in fast 3D imaging are discussed.

OCIS codes: (180.6900) Three-dimensional microscopy; (170.2520) Fluorescence microscopy; (100.6950) Tomographic image processing.

References and links

1. S. Kikuchi, K. Sonobe, and N. Ohyama, "Three-dimensional microscopic computed tomography based on generalized Radon transform for optical imaging systems," Opt. Commun. **123**(4-6), 725–733 (1996).
2. J. Sharpe, U. Ahlgren, P. Perry, B. Hill, A. Ross, J. Hecksher-Sørensen, R. Baldock, and D. Davidson, "Optical projection tomography as a tool for 3D microscopy and gene expression studies," Science **296**(5567), 541–545 (2002).
3. M. Fauver, E. J. Seibel, J. R. Rahn, M. G. Meyer, F. W. Patten, T. Neumann, and A. C. Nelson, "Three-dimensional imaging of single isolated cell nuclei using optical projection tomography," Opt. Express **13**(11), 4210–4223 (2005).
4. M. Oldham, H. Sakhalkar, T. Oliver, G. Allan Johnson, and M. Dewhirst, "Optical clearing of unsectioned specimens for three-dimensional imaging via optical transmission and emission tomography," J. Biomed. Opt. **13**(2), 021113 (2008).
5. M. Rieckher, U. J. Birk, H. Meyer, J. Ripoll, and N. Tavernarakis, "Microscopic Optical Projection Tomography In Vivo," PLoS ONE **6**(4), e18963 (2011).
6. P. Fei, Z. Yu, X. Wang, P. J. Lu, Y. Fu, Z. He, J. Xiong, and Y. Huang, "High dynamic range optical projection tomography (HDR-OPT)," Opt. Express **20**(8), 8824–8836 (2012).
7. E. H. Adelson and J. Y. Wang, "Single lens stereo with a plenoptic camera," IEEE Trans. Pattern Anal. Mach. Intell. **14**(2), 99–106 (1992).
8. M. Levoy, M. Horowitz, R. Ng, A. Adams, and M. Footer, "Light field microscopy," ACM Trans. Graph. Proc SIGGRAPH 2006 25, (2006).
9. G. Saavedra, R. Martínez-Cuenca, M. Martínez-Corral, H. Navarro, M. Daneshpanah, and B. Javidi, "Digital slicing of 3D scenes by Fourier filtering of integral images," Opt. Express **16**(22), 17154–17160 (2008).
10. M. Broxton, L. Grosenick, S. Yang, N. Cohen, A. Andalman, K. Deisseroth, and M. Levoy, "Wave optics theory and 3-D deconvolution for the light field microscope," Opt. Express **21**(21), 25418–25439 (2013).
11. J.-S. Jang and B. Javidi, "Three-dimensional synthetic aperture integral imaging," Opt. Lett. **27**(13), 1144–1146 (2002).
12. Y.-T. Lim, J.-H. Park, K.-C. Kwon, and N. Kim, "Resolution-enhanced integral imaging microscopy that uses lens array shifting," Opt. Express **17**(21), 19253–19263 (2009).
13. L. B. Lucy, "An iterative technique for the rectification of observed distributions," Astron. J. **79**, 745 (1974).
14. W. H. Richardson, "Bayesian-Based Iterative Method of Image Restoration," J. Opt. Soc. Am. **62**(1), 55–59 (1972).
15. J. Juskaitis, R., "Measuring the Real Point Spread Function of High Numerical Aperture Microscope Objective Lenses," in *Handbook of Biological Confocal Microscopy*, Pawley, J.B., ed., 3rd ed. (Springer, 2010).
16. J. W. Goodman, *Fourier Optics*, 2nd ed. (McGraw-Hill, 1996).
17. F. O. Fahrbach, F. F. Voigt, B. Schmid, F. Helmchen, and J. Huisken, "Rapid 3D light-sheet microscopy with a tunable lens," Opt. Express **21**(18), 21010–21026 (2013).

#217354 - $15.00 USD Received 22 Jul 2014; revised 5 Sep 2014; accepted 6 Sep 2014; published 16 Sep 2014

1. Introduction

The recovery of the three-dimensional distribution of fluorescent markers is of paramount importance in a number of intense research fields in Biology and Biomedicine. If the biological samples are small or have been artificially clarified, the spatial distribution of fluorescent protein concentration can be modeled as a collection of incoherent emitters immersed in a weakly scattering medium. Optical Projection Tomography(OPT) [1–4] has been applied to determining these spatial distributions using a set of images of the sample obtained after successive rotations about an axis. Figure 1(a) depicts an OPT system using an afocal lens arrangement adapted to microscopic samples by means of a microscope objective and a tube lens, which compose an optical system with positive magnification. The data are processed in a similar way to conventional X-ray computed tomography data using back projection algorithms [5,6] to reconstruct transverse slices of the sample. However, given that, contrary to X-rays, fluorescent emission takes place in all directions, a restriction must be established to apply computed tomography methods to light sources: as an example, in the optical system depicted in Fig. 1(a), a pinhole has been placed in the Fourier plane to select light traveling parallel to the optical axis to form projection images onto an image sensor. The inefficient use of light in the OPT technique, the need of low numerical apertures, the slow speed of the acquisition process and the complexity inherent in implementing a sample rotation mechanism with a controlled axis of rotation – especially problematic or even impossible for microscopic samples – are the main drawbacks of this technique.

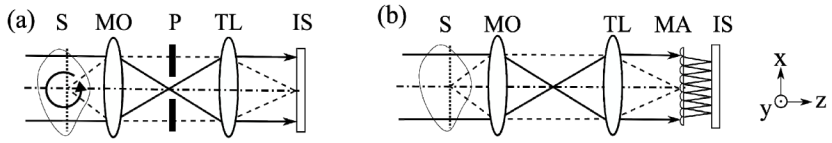

Fig. 1. (a) OPT setup; S sample; MO microscope objective; P pinhole; TL tube lens; IS image sensor. (b) PI setup; MA microlens array.

A different optical imaging technique, closely related with the above, is Plenoptic Imaging (PI) [7], which is based on measuring the light intensity carried by the rays or "light-field" of a geometrical-optics model of image formation. Such light-field determination is made using a microlens array (MA). Figure 1(b) depicts a scheme of a simple implementation of PI in microscopy using, as in Fig. 1(a), an afocal optical system with two components: an infinite corrected microscope objective and a tube lens to form a scaled image of a given plane inside the sample onto a MA. Note that the pinhole (P) is not necessary in this configuration. At a lenslet's focal distance of the MA, an image sensor is placed to detect the intensity distribution of the light traveling along a variety of directions (for clarity only the direction parallel to the optical axis has been depicted arriving to the sensor in Fig. 1(b)), applying the property of the lenses to concentrate the energy of incoming parallel rays with a given angle to points on the focal plane whose lateral position depends on that angle.

Traditionally, the selection and averaging of different collections of pixels in plenoptic images has been used to construct synthetic images in the computer corresponding to different points of view of objects or to views corresponding to different focusing planes in which the out-of-focus part of the scene appears blurred [8,9].

Instead, we propose to use the angular intensity detection capability of the PI method to generate projection images in microscopic samples using a similar approach to that used in OPT reconstruction.

Before detailing our technique, we highlight some important differences between the information provided by both optical approaches. The first is that there is no restriction in the angular range of propagation directions in OPT, since the sample can rotate 360° around the axis perpendicular to the optical axis, but, unless other rotation axes were implemented, the angle variation is restricted to the azimuthal or yaw angle. In contrast, although the angular

#217354 - $15.00 USD Received 22 Jul 2014; revised 5 Sep 2014; accepted 6 Sep 2014; published 16 Sep 2014

range is restricted by the NA of the microscope objective in PI, propagation directions with different pitch and yaw angles can be sampled.

The second difference involves the sampling rate which in OPT is limited by the resolution of the step motor used to rotate the sample and the pixel size of the image sensor. In this sense, it is easy to have a dense data ensemble to feed the reconstruction algorithm by simply taking a sufficient number of acquisitions and using a standard image sensor. In PI the angular sampling is limited by the number of pixels associated to each lenslet and by the lenslet aperture, which captures all the energy arriving inside an oriented volume defined by the lenslet's geometry. In order to obtain sufficient data sampling for back-projection, the MA must meet stringent requirements: ideally, they should be large arrays with a small lenslet aperture size and adequate focal lengths; also the image sensor must have resolution to provide a sufficient number of pixels for each microlens.

Finally, the most relevant difference is that OPT requires at least half the sample to be in focus requiring, unavoidably, the use of low numerical aperture objectives even when imaging at high magnifications. In PI high magnifications with high NA's are not only possible, but offer additional information in the form of a larger span of angular measurements.

Recently, the tomographic reconstruction of fluorescent samples with microscopic resolution has been proposed using a standard PI system based on an extensive computational method [10] with a strong dependence on diffractive optics theoretical modeling of the PI signal expected of point emitters.

Here, we explore a different approach, demonstrating the effectiveness of a back-projection reconstruction algorithm based on a simple geometrical optics modelling of the signal provided by the PI system to obtain microscopic tomographic reconstructions.

To enable the use of the standard MA and image sensor available in our laboratory, and still have a dense data set, a series of images is acquired by scanning the MA in the transversal plane. Even though this process has been proposed before [11,12], its implementation as shown here is novel. In section 2 we show the improvement in angular resolution of this approach, presenting in section 3 the theoretical framework which enables the 3D reconstruction. Sections 4 and 5 show simulations and experiments, discussing our findings and conclusions in Section 6.

2. Improvement of the angular resolution by scanning the microlens array

The signal registered by each pixel in the image sensor of the PI setup corresponds to the integrated energy of the light traveling inside a solid volume in the form of an infinitely long cuboid limited by squared sides corresponding to the microlens aperture (assuming squared lenslets) oriented in space with a certain pitch and yaw (depicted as the dotted lines in Fig. 2(a) for the direction parallel to the optical axis).

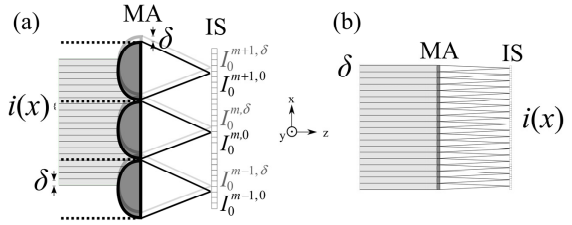

Fig. 2. (a) A plot describing the method of scanning the MA using a low resolution image sensor (IS) to increase the resolution of the angular detection. (b) A static equivalent to (a).

Much finer sampling is possible using these integrated microlens signals by acquiring images after displacing the MA in the transversal plane (the plane defined by the (x, y) coordinates in Fig. (1)). Assuming, for simplicity, a two-dimensional space where only pitch angles are possible, it can be seen that the lateral displacement along the *x*-axis of a distance δ of an array of *m* microlenses allows the acquisition of *m* integrated intensity

#217354 - $15.00 USD Received 22 Jul 2014; revised 5 Sep 2014; accepted 6 Sep 2014; published 16 Sep 2014

values, $I_{\tilde{p}}^{m,\delta}$, for a given angle $\tilde{p}$ different from those obtained before the displacement, $I_{\tilde{p}}^{m,0}$.

Let us define $i_{\tilde{p}}(x)$ as the intensity inside finer cuboids of side δ, in which the microlens-aperture defined cuboids can be divided. If the MA is displaced a number *N* of steps of size δ to reach an accumulative displacement equivalent to the lenslet aperture, and if δ is small enough, the intensity gathered by the microlenses can be represented as the convolution of the high resolution intensity distribution $i_{\tilde{p}}(x)$ and the geometry of the lenslet, $I_{\tilde{p}}(x)=\left[i_{\tilde{p}} * b\right](x)$. In the identity, the function $b(x)$, ideally, would represent a boxcar function. However, taking into account that our MA is a matrix of plano-covex lenslets, we can presume they suffer aberrations, in particular spherical aberration; therefore we model $b(x)$ as an apodization function to account for the fact that marginal rays will contribute less to the intensity measured by the pixel associated to a given angle.

The signal $i_{\tilde{p}}(x)$, can be obtained from the registered set of low resolution images, $I_{\tilde{p}}(x)$, through deconvolution. From the several algorithms existing for this purpose, we obtained good results using the Lucy-Richardson [13,14] deconvolution algorithm. As Fig. 2(b) shows, the signal $i_{\tilde{p}}(x)$ is equivalent to the signal that would be obtained using a MA with the same focal length as the original but with smaller apertures of size δ and a scaled down pixel size image sensor.

3. The reconstruction procedure

The previous deconvolution process generates a set of bidimensional images $i_{(\tilde{p},\tilde{y})}(x,y)$, where $(\tilde{p},\tilde{y})$ represents the pitch and yaw angles of a specific propagation direction that are given by

$$(\tilde{p},\tilde{y})=\left(\tan^{-1}\left(\frac{x'\cos\tilde{y}}{f}\right),\tan^{-1}\left(\frac{y'}{f}\right)\right) \tag{1}$$

where *f* is the lenslet focal length and (x',y') are the image sensor pixel coordinates relative to the lenslets centers.

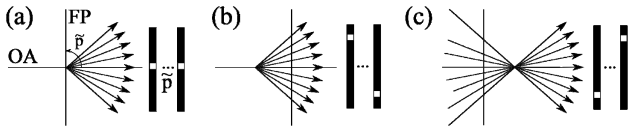

Fig. 3. (a) The set of angular images of an ideal point source in focus for different pitch angles $\tilde{p}$. (b) After the focal plane. (c) Before the front focal plane. OA is the optical axis and FP is the front focal plane of the microscope objective.

Returning to the two-dimensional space, Fig. 3 shows, in a ray-optics scheme, an ideal point emitter generating a distribution of intensity in a plane conjugated with the front focal plane of the microscope objective in which the image sensor (a linear sensor in two-dimensional space) is located. In Fig. 3(a), the emitter is just in focus, and so the expected high resolution image set (the images for the different angles) will consist of a collection of equal images with a single non-zero central pixel. The case represented in Fig. 3(b) now corresponds to the emitter moved away from the focal plane: the image set will be a collection of null images with a non-zero pixel with identical value whose position will vary with the pitch angle. Figure 3(c), shows the emitter closer to the entrance of the optical system and, assuming the same displacement as before but in the opposite direction, the

#217354 - $15.00 USD Received 22 Jul 2014; revised 5 Sep 2014; accepted 6 Sep 2014; published 16 Sep 2014

image set will be the same but in a reverse order. The reconstruction algorithm uses this model for back projection: the elements of a three-dimensional matrix containing the voxels of the reconstructed fluorochrome distribution are obtained by adding the values of the set of pixels in the images $i_{(\tilde{p},\tilde{y})}(x,y)$ associated with the expected pitch and yaw angles corresponding to the voxel coordinates.

4. Simulated results

To demonstrate the procedure, we modeled the image formation process, including the lenslet scanning, generating simulated images that were used to test the back-propagation algorithm. Despite that a high numerical aperture (NA) microscope objective was used in the experimental demonstration described below, we follow the criteria stated in [15]to use scalar diffraction instead of vectorial diffraction. Also, it was assumed that fluorescence emission from a point source can be modeled as a spherical wave whose curvature depends on the emitter axial position with respect to the microscope objective and a diffraction limited optical system.

The field distribution on the microlens plane was modeled as the discrete Fourier transform of the generalized microscope exit pupil function, which includes defocus aberration in an amount related with the distance of the emitter to the front focal plane of the microscope objective. In particular, in the case of an infinity corrected microscope objective, the image of a source located at an axial position z in front of the microscope objective generates an image at the position Z behind the tube lens. The defocus aberration on the exit pupil with a maximum phase at the rim of the exit pupil, W_{m}, is related with Z by the expression [16]

$$W_{\mathrm{m}} = \frac{\pi\omega^2}{\lambda}\left(\frac{1}{Z}-\frac{1}{F}\right) \tag{2}$$

where ω is the radius of the exit pupil, F is the microscope tube lens focal length and λ is the wavelength. Given that we are simulating the microscope as an afocal optical system, the distance from the source to the front focal plane, $\Delta z = f - z$, and the distance between the image and the back focal plane of the tube lens, $\Delta Z = F - Z$, are related by

$$\Delta z = n\Delta Z / G^2 \tag{3}$$

where n is the immersion media refractive index, G is the system magnification, $G = -F/f$, and the pupil diameter radius is given by the expression $\omega = \mathrm{NA}F/G$.

In the numerical simulation, the scale of the Fourier transform is controlled adjusting the ratio between the diameter in pixels of the exit pupil and the size of the matrix where it is inscribed. In particular, an aperture diameter of 80 px inscribed in a 512x512 matrix was chosen in the example shown below.

Once the field at the MA plane is computed, the passage through it (LxL microlenses) is simulated by extracting a collection of complex-valued sub-matrices with dimensions NxN in correspondence with a MA consisting on squared lenslets with fill factor one. The number of MA shifts in each direction, S, was chosen equal to N.

Given that the image sensor is placed in the MA focal plane, the image on this plane is obtained computing the Fourier transform of each sub-matrix. Zero padding to build matrices of larger dimensions MxM, is used to control the scale of the Fourier transforms. The central region, with dimension NxN, is extracted from each transform and stitched to the others to form the simulated camera image. The ratio between N and M determines the microlens focal length and was chosen to avoid cross-talk between microlenses; in the results shown below, N = 20 px and M = 35 px and the number of lenslets L = 25 in each direction.

#217354 - $15.00 USD Received 22 Jul 2014; revised 5 Sep 2014; accepted 6 Sep 2014; published 16 Sep 2014

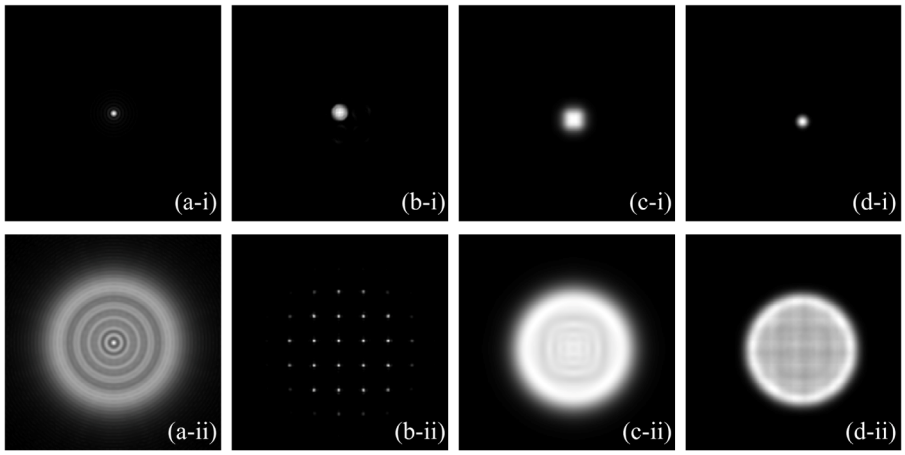

Fig. 4. (a-i) and (a-ii) the intensity on the MA plane for an emitter in-focus and out focus respectively. (b-i) and (b-ii) the intensity on the sensor plane for an emitter in-focus and out-focus respectively for the initial position of the MA. (c-i) and (c-ii) the average of the images for the different displacements of the MA for the in-focus and out-focus emitter. (d-i) and (d-ii) the average of the images corresponding to the different angles for the in-focus and out-focus case respectively. All the images have 200x200 px.

Figure 4(a) shows, as an example, the image corresponding to the intensity distribution on the microlens plane generated by an emitter on the focal plane of the microscope objective (inset i). As can be seen, the first zero of the Airy function occurs at the fourth pixel from the center of the image, which – given that this value must occur at $\lambda G/2\mathrm{NA}$ – defines the size of the pixel as approximately $6\,\mu m$. Figure 4(a-ii) shows an emitter placed out of the microscope objective focal plane, whose intensity distribution was generated using a defocus aberration with a maximum phase of $W_{\mathrm{m}} = 16.11$ rad at the rim of the exit pupil. Using Eq. (2) and 3, this value corresponds to a distance from the focal plane of the microscope objective $\Delta z = -3.2\,\mu m$ assuming G = 100x, NA = 1.3, n = 1.52, $\lambda = 620\,nm$ and F = 200 mm.

Figures 4(b-i) and (b-ii) shows the central region (200x200 px) of the original image (500x500 px) corresponding to the intensity at the image sensor plane for the MA at the start position before shifting when the emitter is on the microscope front focal plane and out focus respectively. Given that, for this particular MA position, the field distribution of the in-focus emitter is approximately centered on a single microlens aperture, the image on the camera is a circular spot with diameter of 16 px (Fig. 4(b-i)). This indicates that the information of the energy carried by a ray with the maximum propagation angle that the microscope objective can capture can be measured using the value of the eighth pixel from the center of each microlens. Then, despite that 20x20 angular values can be extracted, only 16x16 are significant to be used for the reconstruction.

Figure 4(c-i) and (c-ii) shows the average of the images for all the 20x20 shifts for the in-focus and out focus emitters respectively, and Fig. 4(d-i) and (d-ii), shows the central region (200x200 px) of the average of images (480x480 px) corresponding to the different angles (16x16) extracted from the simulated ensemble; again for the in-focus and out-focus cases respectively. It can be observed that, despite diffraction, the angular averages shown in Fig. 4(d-i) and (d-ii) are consistent with a two dimensional version of the scheme shown in Fig. (3), ideally a point and a disk respectively. Returning to the scheme shown if Fig. 2(b), with the parameters used in the simulation, an equivalent ideal (non-limited by diffraction) static MA would have a pitch $\delta \simeq \lambda G/8\mathrm{NA}$ and an image sensor of $\left(L \times N \times S\right)^2$ elements.

#217354 - $15.00 USD Received 22 Jul 2014; revised 5 Sep 2014; accepted 6 Sep 2014; published 16 Sep 2014

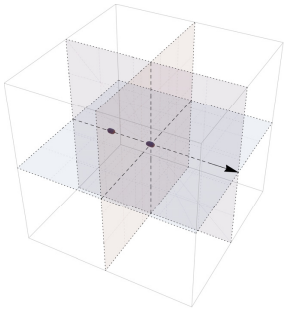

Fig. 5. The reconstruction of the fluorochrome density distribution in the front focal volume of the microscope objective corresponding to two simulated point sources emitting simultaneously, one in-focus (at the cube center) and the other out-focus, obtained from the simulated MA image set of Fig. 4. Only the voxels with value higher than 0.7 of the normalized matrix (300^3 elements) of the reconstruction are represented. The arrow indicates the optical axis and the light propagation direction.

Taking in to account that the imaging formation process with fluorescence is incoherent, in order to simulate the images generated by several emitters present simultaneously in the focal volume, it is only necessary to add the sensor images generated by each one independently. Figure 5 shows the reconstruction obtained from the image set corresponding to the simultaneous presence of the two emitters shown independently in the Fig. 4. This result demonstrates that, in a diffraction-limited system, ignoring diffraction – as the data gathering process of the diffraction images effectively does in order to generate the angular images used to feed the back-propagation reconstruction algorithm – does not impedes a high-resolution reconstruction of the fluorescence distribution.

However, diffraction alone, without considering other losses caused by vignetting present in a real system, produces a loss of the reconstruction intensity through defocus. This was corrected applying a gain as function of the axial coordinate before data normalization.

In addition, it must be noted that the presence of aberrations can compromise the performance of the method. For example, we observe that the introduction of spherical aberration in the generalized pupil function degrades the reconstruction by distorting the expected distribution asymmetrically respect to the focal plane.

5. Experimental demonstration

To demonstrate the principle experimentally, the system depicted in Fig. 6 was built using an inverted commercial microscope (Nikon TE2000-S) as platform. The source for fluorescence excitation was the microscope halogen lamp filtered with a pass-band filter, F1 (Chroma, z532/10x). The microscope objective was an infinity corrected 100x NA 1.3 (Nikon Plan Fluorite) oil immersion objective, which accept angles up to $\pm 60^{\circ}$. After the objective and before the tube lens, an emission filter, F2 (Chroma, HQ620/60x), is used to select the fluorescence light. Given the microscope NA and the observation wavelength, the lateral resolution is $\lambda/2\mathrm{NA}=0.24\mu m$ at most. The MA (OKO-aμs APO-Q-P114-R1.38) is positioned in the image plane of the left microscope camera port (see the scheme on the left of Fig. 6) using a holder that permits rotation, tilt and tip for fine adjustment of the orientation.

#217354 - $15.00 USD Received 22 Jul 2014; revised 5 Sep 2014; accepted 6 Sep 2014; published 16 Sep 2014

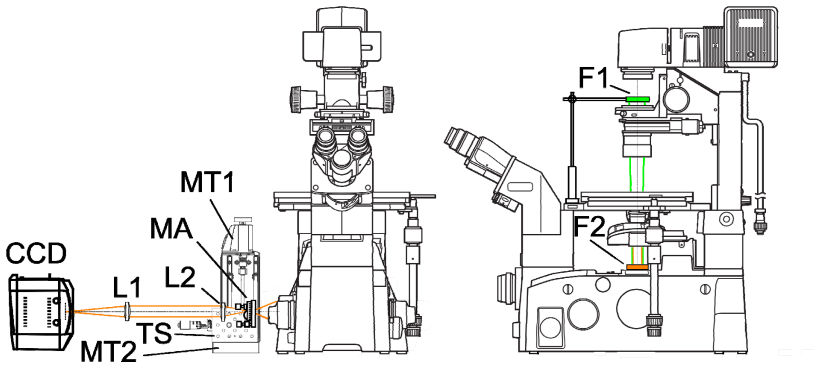

Fig. 6. Scheme of the PI system coupled with an inverted microscope. L1 and L2 are lenses; MA is the microlens array; MT1 and MT2 are linear motorized translation stages; TS is a micrometric translation stage; F1 and F2 are filters.

The MA used here (OKO-aμs APO-Q-P114-R1.38) consisted of a 10x10 mm matrix of squared plano-convex lenslets with 3 mm focal length, 114 μm pitch and fill factor 1, and was placed with the curved side of the lenslet facing the incoming light. The MA holder is coupled to a system of two motorized linear translation stages (MICOS PLS-85 1" SM 1 MLS with SMC pollux I 2SM-Controller), allowing displacement of the MA along the x and y axis, as defined in Fig. 2. We chose $N = 20$ as the number of displacements ($\delta = 5.7\,\mu$m). Two doublet achromats, lenses L1 and L2, of 150mm and 50mm focal length, respectively, reimage the MA focal plane with 3X magnification on to the CCD sensor of the camera (Andor Ixon, 512x512 px; 16x16 μm pixel size). This magnification and the extra space needed for scanning the MA restricts the number of microlenses filling the CCD sensor to an array of 22x22 with 26x26 pixels available for detection under each microlens. Given that the angular range occupies around 14 pixels in each direction, crosstalk between microlenses is discarded. A set of reference images was first acquired for each MA lateral displacement – without the sample and removing the band-pass filter – to determine the centers of the microlenses on the CCD plane; Fig. 7(a) shows as an example the first reference image of the 20x20 set.

To study the system's performance, we made samples consisting of one drop of polystyrene fluorescent microspheres of $1\,\mu$m diameter (Invitrogen, FluoSpheres 540/560) dissolved in agarose and water, cooled down to reach the gel state on a microscope cover slide. As the images in Fig. 7(b-f) shows, due to the low concentration of microspheres, just two are present in the field of view at a distance from the system aperture short enough to be detected. Panel (b) shows, as an example, the image obtained (0.03 sec of exposure time) for the MA initial position while Panel (c) represents the image resulting from the average of the complete set. In this figure, the borders of the microlenses can be seen as a shadow cast by the light removed from the optical system by diffraction and the ringing associated with the combined effect of diffraction and defocus in the microscope.

From the complete set of all displacements, a new set corresponding to the images associated to the different pitch and yaw angles is built. As an illustration, Panel (d) in Fig. 7, shows the image corresponding to the angle defined by the pixels with coordinates $(x', y') = (-4, -1)$ relative to the centers of the microlenses. These images have a dimension (440x440 px) provided by the product of the number of microlenses and the number of motor steps representing one pixel an area of δ on the MA plane. Artifacts can be seen, probably due to the imperfect alignment of the MA plane with respect to the axes of lateral displacement which are also almost certainly not perfectly orthogonal. We found that a Gaussian as function $b(x)$ with variance $N/2$ regularizes largely errors in the acquisition data (this function was also used in the numerical simulation). Figure 7(e) shows the result of

#217354 - $15.00 USD Received 22 Jul 2014; revised 5 Sep 2014; accepted 6 Sep 2014; published 16 Sep 2014

the deconvolution of the image in Panel (d). It can be seen that the spots diameter are in agreement with the microsphere diameter.

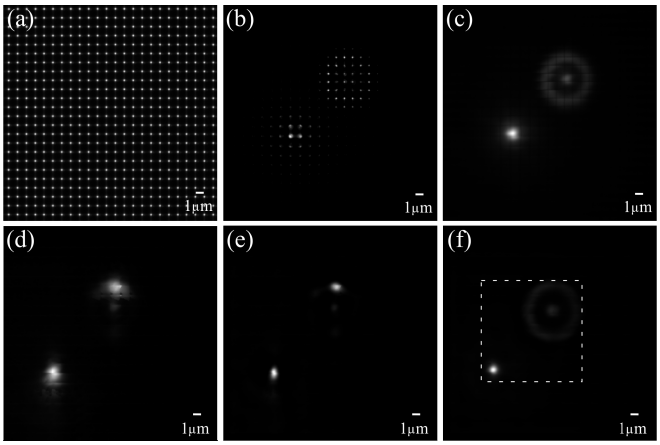

Fig. 7. (a) The reference image corresponding to the MA initial position. (b) The sample, imaged through the MA at the initial position. (c) The ensemble average of the scanning images; (d) One of the low resolution angular images. (e) The deconvolution of (d). (f) The average of the angular images. The bar represents the scale in the sample space.

Figure 7(f) shows the average of the complete set of deconvolved angular images, which is, without taking into account the ringing, consistent with the ray-optics model of one microsphere almost in focus (a point in the model) and the other out of focus (a disc in the model). The disparity between the defocused microsphere images of Fig. 7(b) and (c) and the images of Fig. 4(b-ii) and (d-ii) can be explained by the fact that no ideal point emitters are used here.

The results of the back projection algorithm using the experimental data after applying a Hann filter with cut-off at 20% of the maximum frequency are shown in Fig. 8(a-c). Only a region of 210x210x210 voxels is reconstructed corresponding to the region of 210x210 pixels marked with a dashed square in Fig. 7(f). The intensity was corrected after reconstruction to account for the quadratic varying energy that the microscope objective can capture which depends on the distance of the source to the front lens. The insets (210x210 px) of Fig. 8(b) shows the recovered signal at transversal planes where the maximum local value occurs represented as a gray scale images. Note the moderate elongation of the reconstructed spheres along the axial direction caused by the limited angular range.

While the lateral distance between the microspheres can be established from the value of a pixel in the transversal plane ($1\,\text{px} = \delta/100\ \mu\text{m}$), the measurement of axial distances depends of several not completely determined microscope parameters and needs the system to be calibrated. For this, we used a single microsphere obtained drying a drop of microspheres dissolved in water on a cover slip. Several acquisitions were made for consecutive axial displacements of the sample, moving the fine adjustment knob of the microscope that it is marked with $1\mu\text{m}$ increments. Figure 8(d) shows all the reconstructed microspheres plotted together using different colors for each displacement. The microsphere represented in green was obtained for a plane between two knob marks corresponding to the microsphere axial displacements of the blue and red depicted microspheres. In light of the results we can state that our system provides an axial resolution similar to the lateral and estimates the axial distance between microspheres in the agarose sample at around $5\mu m$. In addition, taking in to account the aforementioned effect that spherical aberration can induce, these results assure that the system does not suffer this aberration.

#217354 - $15.00 USD Received 22 Jul 2014; revised 5 Sep 2014; accepted 6 Sep 2014; published 16 Sep 2014

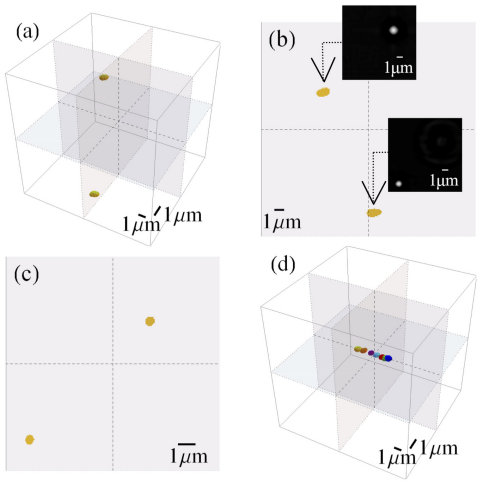

Fig. 8. (a) The reconstruction of the volume in front of the microscope objective of two fluorescent microspheres in agarose; (b) top projection with insets showing the signal on transversal planes at the marked axial positions; (c) the front projection. (d) The reconstruction of a single microsphere in different axial locations around the microscope front focal point (each color represents an independent measurement). The matrices were normalized and a threshold of 0.7 was applied before representation except in the insets in (b) where no threshold was applied.

6. Conclusions

We here describe a method to obtain the three-dimensional distributions of fluorochrome concentration in microscopic unperturbed samples observed from a single direction with high numerical aperture objectives that provide a large enough angular range for a successful reconstruction of a significant volume around the focus.

Reconstruction of the distribution of fluorochromes is possible with a fast filtered back projection algorithm that relies on a simple modeling of the image formation and does not require any interaction with the sample.

The data needed for reconstruction is obtained by acquiring several images either by transversally scanning the Microlens Array (MA) at the image plane in the microscope camera port as done here, or by using a set of lenses to maximize the number of lenslets imaged by a large sensor camera, such as a sCMOS. Our system has the following limitations: the small area and a large lenslet aperture of the MA; and the low lateral resolution of the image sensor. By scanning the MA, these limitations can be circumvented, permitting us to gather the same data that would be obtained with one-shot static ideal (non limited by diffraction) MA with $114/20\,\mu$m pitch in front of a very high resolution 8800x8800 px image sensor.

The step motors used are not ideal for the kind of short range displacement required and system operation could be much faster using piezoelectric positioners to increase the scanning speed and reducing the camera exposure times to reduce the complete acquisition time to a few seconds.

The current technology for microptics manufacture is constantly advancing and it is not unrealistic to foresee the availability of extended areas of lenslets with smaller pitch – although diffraction will impose a limit – and controlled curvatures. These dense sampling MAs will need to use high resolution and high efficiency image sensors that are expensive but already available. Once these characteristics are meet, the traveling distance and the number of steps when scanning the MA will be reduced and the described back propagation could operate with data obtained with less acquisitions, offering real time fluorescence tomographic

#217354 - $15.00 USD Received 22 Jul 2014; revised 5 Sep 2014; accepted 6 Sep 2014; published 16 Sep 2014

reconstruction, which could represent an extremely valuable tool for imaging fast processes at high resolution, such as the beating heart of a zebrafish [17].

Acknowledgments

This work was supported by the Spanish MINECO grant DPI2012-32994. JR acknowledges support from Marie Curie CIG "High-Throughput Tomo" and Spanish MINECO grant FIS2013-41802-R. We wish to thank Prof. Manuel Martinez-Corral for helpful discussions on plenoptic imaging.

#217354 - $15.00 USD Received 22 Jul 2014; revised 5 Sep 2014; accepted 6 Sep 2014; published 16 Sep 2014